Beyond single-crystal surfaces: The GAL21 water/metal force field

Paul Clabaut, Matthieu Beisert, Carine Michel, Stephan N. Steinmann

Beyond single-crystal surfaces: The GAL21 water/metal force field

Paul Clabaut,[1, a)] Matthieu Beisert,[1] Carine Michel,[1] and Stephan N. Steinmann[1, b)]
Ecole Normale Supérieure de Lyon, CNRS, Laboratoire de Chimie UMR 5182, 46 allée d'Italie, F-69364, LYON, France

(Dated: 28 October 2022)

Solvent effects are notoriously difficult to describe for metallic nano-particles (NPs). Here, we introduce GAL21 the first pair wise additive force field that is specifically designed to modulate the near chemisorption energy of water as a function of the coordination numbers of the metallic atoms. We find a quadratic dependence to be most suitable for capturing the dependence of the adsorption energy of water on the generalized coordination number (GCN) of the metal atoms. GAL21 has been fitted against DFT adsorption energies for Cu, Ag, Au, Ni, Pd, Pt, and Co on 500 configurations and validated on about 3000 configurations for each metal, constructed on five surfaces with GCNs varying from 2.5 to 11.25. Depending on the metals, the RMSD is found between 0.7 kcal·mol^{-1} (Au) to 1.6 kcal·mol^{-1} (Ni). Using GAL21, as implemented in the open-source code CP2K, we then evaluate the solvation energy of Au_{55} and Pt_{55} NPs in water using thermodynamic integration. The solvation free energy is found to be larger for Pt then for Au, and systematically larger than 200 kcal·mol^{-1}, demonstrating the large impact of solvent on the surface energetics of NPs. Still, given that the amorphous NPs are both, the most stable and the most solvated ones, we do not predict a change in preferred morphology between the gas-phase and in water. Finally, based on a linear regression on three sizes of NPs (from 38 to 147), the solvation energy for Au and Pt surface atoms are found to be -5.2 and -9.9 kcal·mol^{-1}, respectively.

I. INTRODUCTION

Metallic nanoparticles (NPs) have unique properties related to the nature of the metal but also their morphology and the exposed surface sites, which can be tuned and modified when used in an aqueous medium. Their ability to diffuse through the human body to reach the treatment site,[1] combined with their radio-sensitising properties that could be used to selectively kill cancerous cells[2] make them appealing in teragnostic. In catalysis and electrocatalysis,[3] the unique reactivity of their surface sites is exploited by enhancing the surface-over-volume ratio to maximise the exposed surface area while minimising the total amount of necessary noble metal catalysts. This has led to a global augmentation of the dispersion of active catalyst on support surfaces and, thus, to a reduction of the size of the metallic nanoparticles.[4–6]

The usage of NPs in the biological environment and in many (electro)-catalytic processes implies interactions between the nanoparticles and liquid water that may result in changes in morphology and exposed active sites. However, simulating metallic nanoparticles in water is very challenging: simulations of hundreds of atoms constituting the nanoparticles along with the corresponding (large) water phase would be required. Few studies exist that perform such simulations at the computationally costly ab initio level, although the literature is rather rich regarding the simulation of the corresponding single-crystal surfaces.[7]. As examples, we can mention photo-activated water splitting on small Ru clusters[8] and O_2 dissociation on small Au particles[9]. In both studies, the small clusters have been supported on a solvated oxide surfaces. Other studies investigate directly the nanoparticle/water interface structure with heavy simulations but are limited to structure optimisation,[10] implicit solvation,[11] or short sampling duration.[12] Molecular mechanics (MM) simulations could be employed to lower the cost of the sampling. However, adapted force fields that deliver relevant structures and surface solvation for nanoparticles hardly exist. Jacob and co-workers recently investigated the oxidation and degradation of Pt clusters under (electro-)oxidation conditions using ReaxFF.[13] They benefited from an intense parametrization and validation effort in the past decade[14] that is not available for many metals and adsorbates. To reach a more transferable description, a simpler functional form is desired that is compatible with "standard" force fields. However, describing the interaction between two different classes of materials like a metallic nanoparticle on one hand and liquid water on the other hand poses several challenges. The near-chemisorption of water needs to be properly described in terms of energy, adsorption site and orientational preference of water relative to the local surface of the NP.[15] We recently proposed GAL, a metal/water force field that includes an angular dependence and an attractive Gaussian to localize the water on the appropriate adsorption site on a Pt(111) surface.[16] Since GAL17 captures the near-chemisorption of water on Pt(111), it is able to describe the competition for adsorption sites between the solvent and other adsorbates. Therefore, GAL17 was used to assess the impact of solvation on the adsorption energy of aromatic molecules on Pt(111), leading to a semi-quantiative agreement with experiment.[17] Indeed, for the determination of solvation

[a)] Also at Université Gustave Eiffel, DGD Informatique et Numérique, 5 Boulevard Descartes, 77454 Marne-la-Vallée, France
[b)] Electronic mail: stephan.steinmann@ens-lyon.fr

energies of adsorbates on (metal) surfaces, our strategy relies on the combination of interfacial force fields for the interaction between the solvent and the surface, with a "standard" (typically UFF)[18] force field for the description of the adsorbate. For all these simulations, the DFT subsystem (surface plus adsorbate) are kept frozen, i.e., no force field is required for these interactions that are generally difficult to describe.

Based on our initial work on GAL17,[16] a Pt(111)/water force field that reproduces the corrugation of the potential energy surface (top, hollow, bridge sites) of water on Pt(111), we have recently introduced the GAL19 force field to describe water/metal (alloy) surface interactions.[19] The main ingredient beyond the standard physisorption potentials[20] is the angular dependence of the interaction between the water dipole moment and the surface norm, supplemented by an attractive Gaussian potential. However, GAL19[19] is only parametrized for the (100) and (111) perfectly flat crystal surfaces. The metallic environment of atoms in such extended surfaces differs from the environment of exposed metallic atoms at the surface of nanoparticles. At the centre of flat exposed portions of the surface, the chemical environment of the metallic atoms might resemble (100) or (111) facets but this does not hold true for edges or corner atoms. The diversity of surface atoms on nanoparticles asks for a unified force field that explicitly depends on the local topology in order to capture the modulation of the near-chemisorption interaction.

In 2014 Calle-Vallejo *et al.* introduced the generalised coordination numbers (GCN) to correlate the adsorption energy of atoms and small molecules on nanoparticles with the metallic environment of the surface atoms.[21,22] The GCN can be seen as a second-order corrected coordination number, as the information of the incomplete coordination sphere of atoms is propagated to/from its first neighbours. GCNs are, therefore, much more sensible to the local surface environment than standard coordination numbers. Even though GCNs do not perfectly capture the variations of adsorption energies on various sites of small nanoparticles,[23] the GCN is a low-cost, physically motivated descriptor that captures overall trends.[24] Therefore, we decided to exploit the GCN for the development of a unified metal/water force field for arbitrary metal surfaces and nanoparticles.

We here develop the GAL21 force field, which re-uses the functional form of GAL19 but introduces a continuous dependence of the parameters on the GCN of the metallic atoms. By parameterising the force field on a set of DFT interaction energies of water molecules on metallic surface atoms featuring a wide range of GCNs, a unified functional form, adapted to any kind of surface or particle, is obtained.

II. STRUCTURE-SENSITIVITY OF THE ADSORPTION OF A WATER MOLECULE ON A METALLIC SURFACE

We aim at developing a force field that is able to describe the metal/water interaction when the metallic atom belongs to a particle. As a preliminary study, we evaluated at the DFT level (see computational details) the adsorption of a water molecule on a series of metallic periodic slabs, varying the metal (Cu, Ag, Au, Ni, Pd, Pt, Co), the type of facets ((111) and (100)), and the presence of ad-atoms or defects. The different model surfaces and atomic sites considered are shown in Fig 1.

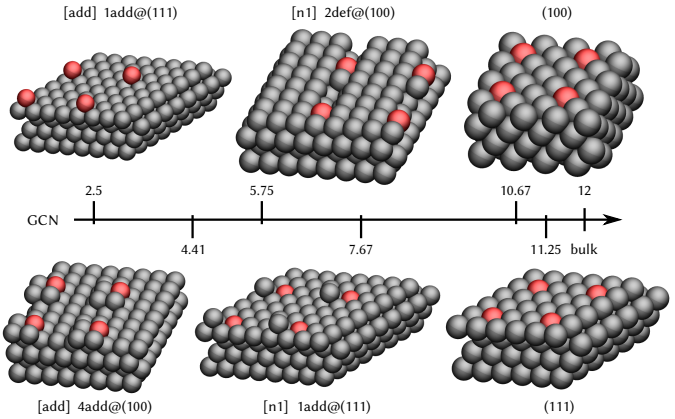

FIG. 1: 2×2 super-cell representations of the model slabs and atomic adsorption sites chosen for this study. Red atoms represent the atomic sites on top of which water molecules are adsorbed. A Generalized Coordination Number (GCN) and a name is associated with each of these atoms. Between brackets are the specific names of the atomic sites on the slabs, followed by the designation of the slabs themselves. Atomic site names are not mentioned when all the surface atoms of a slab are identical. [add] stands for the addatoms, [n1] stands for the first neighbour of an addatom or defect ; $n$add@S stands for a surface S with n addatoms, while $n$def@S stands for a surface S for whom n atoms were removed.

To characterize the local topology of a given metallic site, we have chosen to use the generalized coordination number (GCN).[21] The generalised coordination number $GCN(i)$ of a metallic atoms i is computed according to:

$$GCN(i) = \sum_{j}^{n} \frac{CN(j)}{CN_{max}} \quad (1)$$

where the summation runs on its n closest neighbours, $CN(j)$ is the standard coordination number of the neighbour j, and CN_{max} is the maximum coordination number (CN corresponding to a complete coordination sphere) that could be reached for an atom situated in a bulk metal of the same nature (12 for an fcc metal). A visual summary of the method is provided in Fig 2.

The determination of the neighbours and of their coordination number is not uniquely defined for general (e.g., amorphous) systems and is, here, performed by the parameter-free ASANN algorithm.[25] In Fig. 1, the GCN of the adsorption site (highlighted in red) is provided. It spans a wide range, from 2.5 to 11.25 (12 being the maximum in the bulk).

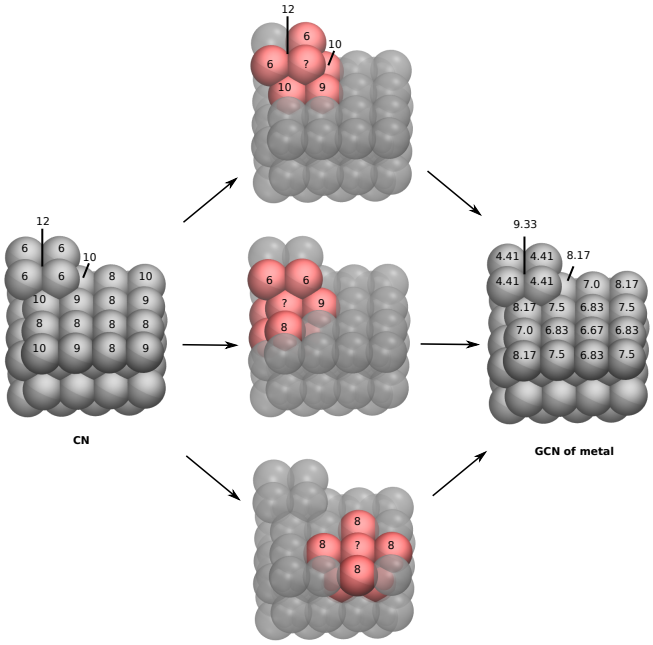

FIG. 2: Schematic representation of the GCN determination process. On the left, the standard coordination numbers of the metallic atoms. As a first step, the neighbour of each atom are identified and their standard coordination numbers gathered. In a second step, the formula is applied to compute the GCN of each metallic atom of the slab.

The adsorption energy of a water molecule $E_{ads,min}$ is defined as:

$$E_{ads,min} = E_{H_2O@slab} - E_{H_2O} - E_{slab} \tag{2}$$

with $E_{H_2O@slab}$ the energy of the adsorption of a water molecule on the selected atomic site on the slab, E_{H_2O} is the energy of the isolated water molecule and E_{slab} is the energy of the slab. The relation between the DFT minimum adsorption energies on the various explored adsorption sites and the GCN of the nearest atomic adsorption sites is presented in Fig 3. The adsorption energy is not linearly but rather quadratically dependent on the GCN. This information is key to motivate the GAL21 functional form.

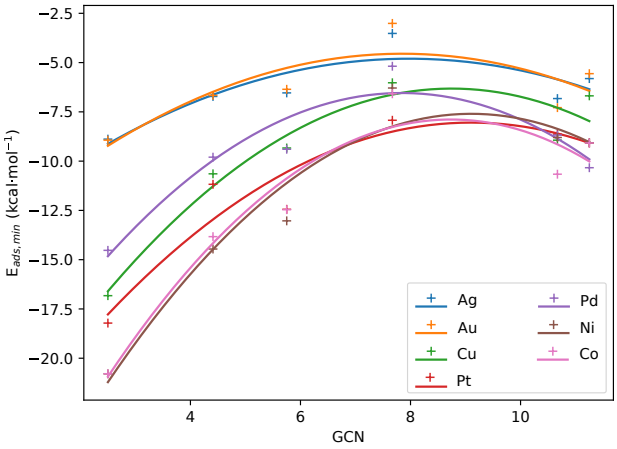

FIG. 3: DFT minimum adsorption energies of water among the configuration set used in this study for each atomic adsorption site in function of the GCN of the atomic adsorption site and the corresponding fitted parabolas.

III. DEVELOPMENT OF A STRUCTURE-SENSITIVE METAL-WATER FORCE FIELD

A. GAL21 functional form

The basic atom-pairwise additive functional form of GAL19[19] was used:

$$\begin{aligned} V_{\mathrm{GAL19/21}} = &\sum_{H} \sum_{M\in\Omega(H)} \mathrm{V}_{M,H}(\vec{r}_{M,H}) \\ &+ \sum_{O} \sum_{M\in\Omega(O)} \mathrm{V}_{M,O}(\vec{r}_{M,O},\theta) \end{aligned} \tag{3}$$

where $\Omega(H)$ and $\Omega(O)$ represent two ensemble of metallic atoms (indistinct of their nature in the case of an alloy) within a given distance cut-off of an H atom and the O atom respectively.

The interaction of the surface with the hydrogen ($V_{M,H}$) atom is purely repulsive:

$$\mathrm{V}_{M,H}(r_{M,H}) = A_H e^{-r_{M,H}\cdot B_H} \tag{4}$$

where r is the norm of $\vec{r}$, A_H tunes the strength of the repulsion, and B_H (an inverse distance) describes the characteristic distance of the exponential decay.

The attractive interactions between water and the metal surface are collected in the oxygen/metal interaction potential:

$$\begin{aligned} \mathrm{V}_{M,O}(\vec{r}_{M,O},\theta) = &\mathrm{V}_G(\varepsilon_a, b_{\parallel}, b_{\perp}; \vec{r}_{M,O}) \\ &+ \mathrm{V}_A(R_O, a_{1-4}; r_{M,O}, \theta) \\ &+ \mathrm{V}_{TT}(A, B, C_6; r_{M,O}) \end{aligned} \tag{5}$$

where V_G is an attractive Gaussian potential:

$$V_G(\vec{r}_{M,O}) = \varepsilon_a e^{-b_\parallel \cdot r_\parallel^2} e^{-b_\perp \cdot r_\perp^2} \quad (6)$$

where $r_\parallel$ and $r_\perp$ are, respectively, the parallel and perpendicular projection of $\vec{r}_{M,O}$ on the surface normal $\vec{n}$.

V_A is an angular correction term which modulates the interaction energy of the water molecule as a function of the angle θ between the surface norm $\vec{n}$ and the molecular dipole moment:

$$V_A(r_{M,O}, \theta) = \frac{(e^{-r_{M,O}/R_O})^2}{\sum\limits_{M_i \in \Omega(O)} e^{-r_{M_i,O}/R_O}} \sum_{n=1}^{4} a_n \cos(n\theta) \quad (7)$$

where R_O is a parameter for the characteristic distance of the M-O distance and the a_n are the expansion parameters of the Fourier series.

Finally, V_{TT} is the potential of Tang and Toennies,[26] accounting for both the short-range repulsion and the long-range dispersion interactions.

$$V_{TT}(r) = Ae^{-B\cdot r} - \left[1 - \sum_{k=0}^{6} \frac{(B\cdot r)^k}{k!} e^{-B\cdot r}\right] \frac{C_6}{r^6} \quad (8)$$

where A, B, and C_6 are parameters.

The surface normal $\vec{n}$ is defined locally for each metallic atom M of a surface or a nanoparticle. Its definition has been slightly revised compared to GAL19 to behave more smoothly at the surface of highly corrugated objects. It reads:

$$\vec{n}(M) = \sum_i \frac{\vec{r}_{M_i,M}}{r^5_{M_i,M}} \quad (9)$$

where i runs over all metallic atoms (*i.e.*, including all constituents in the case of an alloy) within a distance cut-off of M. The cutoff is defined as the global force field cutoff. The sum causes the resulting vector to point away from the volume containing metallic atoms, and therefore, to the outside of the metallic object.

In total, V_{GAL} depends on 13 parameters: A_H, B_H, ε_a, $b_\parallel$, $b_\perp$, R_O, the four a_n, A, B and C_6. In GAL21, two parameters are taken as GCN-independent (R_O and C_6), six parameters become linearly dependant on the GCN of M: A_H, B_H, $b_\parallel$, $b_\perp$, A, and B; and 5 parameters become quadratically dependant on the GCN of M: ε_a and the four a_n. Each parameter L depending linearly on the GCN of M is written as:

$$L = L_{(1)} \cdot GCN(M) + L_{(0)} \quad (10)$$

and each parameter Q depending quadratically on the GCN of M is parametrized as:

$$Q = Q_{(2)} \cdot GCN(M)^2 + Q_{(1)} \cdot GCN(M) + Q_{(0)} \quad (11)$$

B. Fitting method and data set

In order to investigate atomic sites for water adsorption presenting a wide range of associated GCN, several surfaces were built. Fig 1 presents the different model surfaces and atomic sites considered, along with their associated GCN.

In total, 29 adjustable parameters are needed for the GAL21 force field for each metal: there are four hydrogen repulsion parameters, i.e., the two parameters for the linear dependence of A_H and R_H of Eq. 4. Then, we have seven parameters for the Gaussian attraction (Eq. 6): the three parameters of the quadratic dependence of ε_a and the four parameters of the linear dependence of $b_\parallel$ and $b_\perp$. The angular dependence (Eq. 7) requires thirteen parameters: R_O, and the three parameters of the quadratic dependence of each a_1, a_2, a_3, and a_4. Finally, the physisorption potential (Eq. 8) depends on five parameters: the C_6 coefficient and the two parameters of the linear dependence of A and B).

Like for GAL19, the C_6 parameter is the only one that is not fitted but directly extracted from the DFT computations via the use of the dDsC dispersion correction.[27] In order to fit the remaining parameters, a set of 4154 configurations is built for Co, Ni, Cu, Pd, Ag, Pt, Au. All configurations consist of a single water molecule adsorbed on a p(3×3) or p(4×4) metallic slab. The configurations probe various orientations, distances, and adsorption sites (top, hollow, addatom, etc...) of the water molecule. For each surface, several adsorption sites were identified. Then, for each adsorption site, the potential energy is scanned on a grid, varying the distance to the surface and the angular orientation (θ, ϕ). Only a restricted part of the total set (500 configurations obtained from a stratified random sampling) is used to fit the data, while all geometries with negative adsorption energies are used to validate the model. More details about the set can be found in the supporting information section S1.

Similarly to our previous work,[19] the optimisation process is split between linear and non-linear parameters. Indeed, only nine parameters are non-linear and have been optimized via a simplex optimizer. All linear parameters for which a GCN dependence is introduced can be decomposed into three individually linear (and thus, easy to fit) parameters:

$$\begin{aligned} Q(GCN)\cdot T &= (Q_{(2)} \cdot GCN^2 + Q_{(1)} \cdot GCN + Q_{(0)}) \cdot T \quad (12) \\ &= Q_{(2)} \cdot GCN^2 \cdot T + Q_{(1)} \cdot GCN \cdot T + Q_{(0)} \cdot T \end{aligned}$$

where Q is a linear parameter with a quadratic GCN dependence, $Q_{(i)}$ its components in the GCN dependence, and T a term of the potential. Hence, at each iteration of the simplex, the linear parameters are determined via a least-squares fit. The final parameters have been selected among 18 simplex runs that have been intialized via a Latin hypercube with random values that minimize the maximum correlation coefficient as implemented in pyDOE.

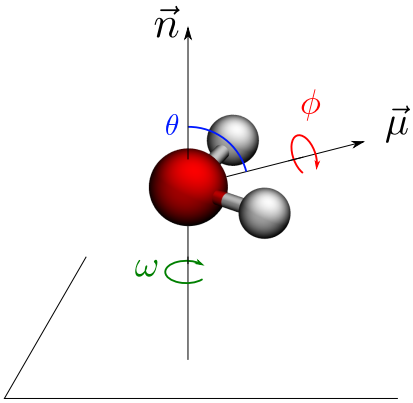

FIG. 4: Schematic representation of the cartwheel angle θ, the propeller angle ϕ, and the helicopter angle ω, defining the orientation of the water molecule with respect to the surface. $\omega = 0$ is arbitrarily defined as a coincidence of the dipole moment vector and the x-axis. At $\phi = 0$ the molecular plane of H_2O is parallel to the surface.

The optimal parameters for the seven metals are provided in Table I.

IV. COMPUTATIONAL DETAILS

All DFT energy evaluations have been carried out with VASP 5.4.1,[28,29] using the PBE generalized gradient approximation functional[30] with the dDsC dispersion correction[31,32] and an energy cutoff of 400 eV for the expansion of the plane-wave basis set. The electron-ion interactions are described by the PAW formalism.[33,34] The interatomic distances of the bulk metals have been optimized and found to be 2.48, 2.49, 2.56, 2.78, 2.92, 2.81, 2.94 Å for Ni, Co, Cu, Pd, Ag, Pt, and Au respectively. Series of 4154 configurations of a single water molecule adsorbed on a p(3×3) (for (100), (111) surface) or p(4×4) (for all the other surfaces) unit cell with 4 metallic layers were built for each of the metals. The slabs are separated by a vacuum of 20 Å in order to minimize interactions between periodic images. The diverse set (see section S1 in the supporting information) explores the configurational space characterised by the four main descriptors: The adsorption site, the distance to the surface, the cartwheel angle θ and the propeller angle ϕ as defined in Fig. 4.

The Brillouin zone was sampled by a Γ-centered 3×3×1 Monkhorst-Pack K-point grid.[35] Idealized geometries (as cut from the bulks) were adopted for the metallic layers, while the water molecule was taken from a DFT optimization in gas phase (O-H: 0.98 Å and a H-O-H angle of 105.32°).

The initial geometries of the Au_{55} NPs have been obtained from the literature[36] and re-optimized at the PBE-dDsC level in VASP with a Fermi-smearing of 0.025 eV (∼ 300 K) in a cubic box of 25 Å. The Fermi smearing at room temperature was chosen to limit the electronic smearing in these molecular systems that feature a gap, in analogy to our studies on semi-conductors.[37] The Pt_{55} NPs have been optimized based on the Au_{55} geometries using analogous settings.

Molecular mechanics simulations have been carried out with a modified version of CP2K 5.1,[38,39] and CP2K 9.1 (which contains GAL21 by default) using the FIST module under periodic boundary conditions. Long-range Coulombic interactions were evaluated through the smooth particle-mesh Ewald summation[40] with roughly 1 mesh point per Å. Molecular dynamics were run in the NpT ensemble at 1 bar, 298 K, using the default settings for the Canonical Sampling through Velocity Rescaling (CSVR) thermostat[41] and default (isotropic) barostat. The geometry of the NPs have been kept fixed in their DFT geometry. In order to ensure that their geometry is not rescaled by the barostat, slight modifications in the source code were required. The TIP3P water model was used for water-water interactions[42] and inter-atomic distances were constraint via the SHAKE algorithm. Note, however, that the nature of the water model has no impact on the GAL21 parametrization. Hence, GAL21 is compatible with all established water models. The water/metal interactions were described by our implementation of the GAL21 force-field. The time step has been set to 2 fs for all MD simulations. The NPs have been solvated exploiting the tleap program from AmberTools, adding ∼ 10 Å of water in each direction. This resulted in nearly cubic boxes of ∼ 30 Å, corresponding to about 3000 water molecules.

For the thermodynamic integrations, 21 windows (ranging from 0.0035 to 0.995) of 200 ps each have been performed. Only the last 100 ps have been used for analysis in order to allow the system to equilibrate. The thermodynamic integration has been performed relying on the blocking algorithm of Flyvbjerg[43] as implemented in *pyblock* and the uncertainties (including for the linear extrapolation to 0 and 1 endpoints) have been propagated by the *uncertainties* python module. The numerical integration itself has been performed via the trapezoidal rule as implemented in *numpy*.

V. RESULTS AND DISCUSSION

A. Performances on crystal surfaces

GAL21 was fitted on 500 randomly-selected single-molecule adsorption configurations with negative adsorption energies that span the diversity of the data set. The root mean square deviation (RMSD, see Table I) was then assessed for all the configurations with negative adsorption energies. The RMSDs span a range between 0.72 (Au) to 1.58 (Ni) kcal·mol^{-1}, which is roughly related to the typical strength of the interaction of water with the corresponding metal (see Fig. 3 for the minimum adsorption energies). In other words it is more the

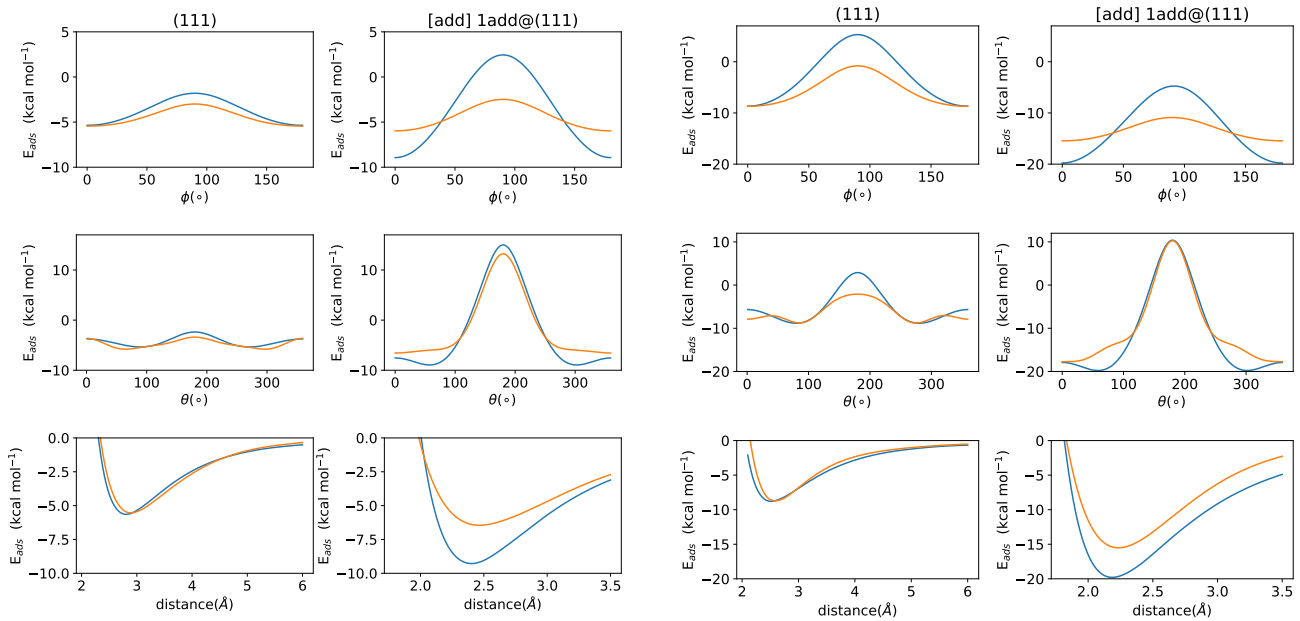

(a) Au

(b) Pt

FIG. 5: ϕ, θ and distance dependence of the adsorption energy on the top site of the (111) facet and the single add atom on the (111) facet (1st and 2nd column) for Au (left) and Pt (right). Blue and orange refer to DFT and GAL21, respectively.

relative accuracy that is preserved when comparing the metals than the absolute one, which is best seen when visually inspecting the parity plots for the different metals (Fig. S2). In turns out that in particular the strongest binding site (low GCN, i.e., the [add] 1add@(111) site) is difficult to consistently capture, despite the attractive Gaussian. We presume that this is due to a coupling between the Gaussian attraction and the orientational dependence that is absent in the GAL21 functional form.

As representative examples we analyse in more detail characteristic angular and distance dependencies for Au (weak binding) and Pt (strong binding). We start with the corrugation between the top (most stable), bridge (less stable) and hollow (least stable) site on the (111) surface. This corrugation is difficult to reproduce by force fields, since the Lennard-Jones potential[20] (or related pair-wise additive physisorption potentials[44]) erroneously assign the adsorption minimum to the hollow site.[45] Figure S1 clearly shows that GAL21 retrieves the relative stability quite well, even though the minimum distance for the less stable bridge and hollow positions are, especially for Pt, somewhat underestimated compared to DFT. Comparing to the other metals (Fig. S3) confirms that this is a quite general trend.

Moving to the angular and GCN dependence, Fig. 5 reveals that the angular dependence is very well reproduced on the (111) site, assigning the maxima to the correct angles. The qualitative agreement is still present for the add-atom adsorption site, but the ϕ dependence, which is governed by the rather simple H-repulsion term of Eq. 4, is not sufficiently pronounced in GAL21 compared to DFT. This, together with the parity plots discussed above, points to a lack of coupling between the angular dependence and the Gaussian attraction: in GAL21 only the GCN introduces some coupling between them, but this is clearly not enough for a quantitative agreement across all the sites. Note that the GCN dependence for Au is only weak (and not perfectly reproduced by GAL21), while on Pt the adsorption energy drops from -8.7 to -19.8 kcal·mol^{-1} at the DFT level, which is qualitatively captured by GAL21 (-8.7 and -15.2 kcal·mol^{-1}).

Minima of the potential energy surface are important since they correspond to the most likely configurations. Considering all the (local) minima on the various surfaces, Fig. 6 shows that the minimum energy sites are faithfully reproduced, even though the very strongly adsorbing sites (< 15 kcal·mol^{-1}) slightly misplace the minimum. This is actually a general observation, i.e., the DFT minimum is frequently found to be slightly less stabilized in GAL21, while the GAL21 minimum is generaly close to the bisector.

In summary, GAL21 provides a consistent performance across the board for low-coverage adsorption energies of water on periodic surfaces, even when accounting for add-atoms and defects.

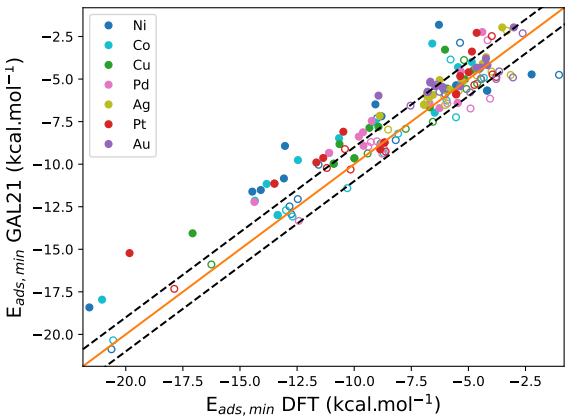

FIG. 6: Parity representation (GAL21 vs. DFT) of the minimum adsorption energy of water on each metal for each of the 12 tested positions. The DFT energy is compared with the GAL21 energy (i) when water is located on the DFT minimum (full symbols) (ii) when water is located on the GAL21 minimum (open symbols). Hence, if they are identical, only one dot is visible. The orange line indicates the perfect parity line, while the dashed lines are shifted 1 kcal·mol^{-1} up or down.

B. Water molecule mono-adsorption on Gold and Platinum nanoparticles

Having established that GAL21 accurately captures the effect of surface roughness on the adsorption energy of water, we move on to a challenging validation set: adsorption energy configurations on small (55 atoms) nanoparticles of gold and platinum.

The five tested morphologies are found to be minima at the DFT level and are represented in Fig. 7. For Au_{55} the two amorphous (Amo1 and Amo2) nanoparticles are close in energy (< 5 kcal/mol), while for Pt the energy difference is ten times higher, in favor of the "flatter" Amo2 NP. Interestingly, the crystalline NPs are all considerably higher in energy (in agreement with previous reports[36]). The "ideal" cuboctahedron (cubo), which is predicted to be most stable for the large-size limit of NPs,[46] is the least stable one, followed by the Ino-type decahedron, while the highly symmetric icosahedron shows intermediate stability. Note that the relative stability is the same for Au_{55} and Pt_{55}, but the relative energy differences are more pronounced for Pt. This flatter energy-landscape of the Au clusters is in qualitative agreement with the macroscopic ductility of Au.

We have constructed a set of geometries of single water adsorption on these NPs based on a GAL21 molecular dynamics trajectory from which snapshots have been extracted. Then, only water molecules with a maximum distance of 3.5 Å between the oxygen atom and the nearest metal atom have been retained. For each single water adsorption case, single-point DFT computations have been performed and only geometries with negative adsorption energies in GAL21 and DFT have been included in Figure 8 to focus on the most relevant structures. The qualitative behavior of the GAL21 description of water adsorption on Au_{55} and Pt_{55} is similar: the lower triangle (stronger adsorption in GAL21 than in DFT) is quite populated, while the upper triangle is empty. As a point of comparison, we show in Fig. S5 the corresponding plot with GAL19 parameters taken from the (111) surface. In contrast to GAL21, GAL19 underbinds water molecules on these under-coordinated sites, which is understandable, as all metal atoms are considered equal and highly coordinated. There are two factors that contribute to the overestimation of adsorption energies of GAL21 for water molecules on these NPs. On the one hand, this is related to the too "flat" ϕ dependence for the undercoordinated sites (see Fig. 5). On the other hand, the significant errors for some of the Amo1 and especially Amo2 configurations originate from the generalized coordination number. The amorphous NPs have a unconventional, non-closed-packed structure, with the "joint" between the surface and sub-surface atoms being non-syntactic. Therefore, they feature GCNs that are quite low (down to 3.1 for Amo1, see Fig. S7). As a consequence, the coordination environment of some surface atoms of Amo1 and Amo2 look rather "complete" from a top view, but subsurface atoms are missing, so that the GCN reaches low (∼3) values. Especially for Pt the low GCN is directly related to low adsorption energies in GAL21, leading to large (>5 kcal·mol^{-1}) errors for Amo2. In other words, the same GCN reflects different electronic structure realities, depending on the crystallinity of the considered system. Note that a similar "breakdown" of a good correlation between the GCN and adsorption energies has already been reported for CO adsorption on an amorphous Au_{38} NP.[23] For the compact icosahedron and, to a lesser extent, the cuboctahedron, the agreement between GAL21 and DFT is, however, satisfying, demonstrating the reasonable transferability between single-crystal surfaces and NPs as long as they are closed-packed, so that their GCNs are comparable. Additional validations in the SI (see Fig. S9) demonstrate a similar accuracy (RMSD of ∼ 1 and 5 kcal·mol^{-1} for Au and Pt, respectively) for a smaller crystalline NP (38 atoms) and three crystalline isomers of larger NPs (147 atoms).

C. Solvation energies of Gold and Platinum nanoparticles

Having established a reasonable accuracy of GAL21 for the interaction between water and nanoparticles, we are now turning to the determination of the solvation energy of Au_{55} (weak water adsorption) and Pt_{55} (strong water adsorption) nanoparticles. As a first step, we have analyzed the number of water molecules that are in the first solvation shell (see Fig. S8). The first observation is

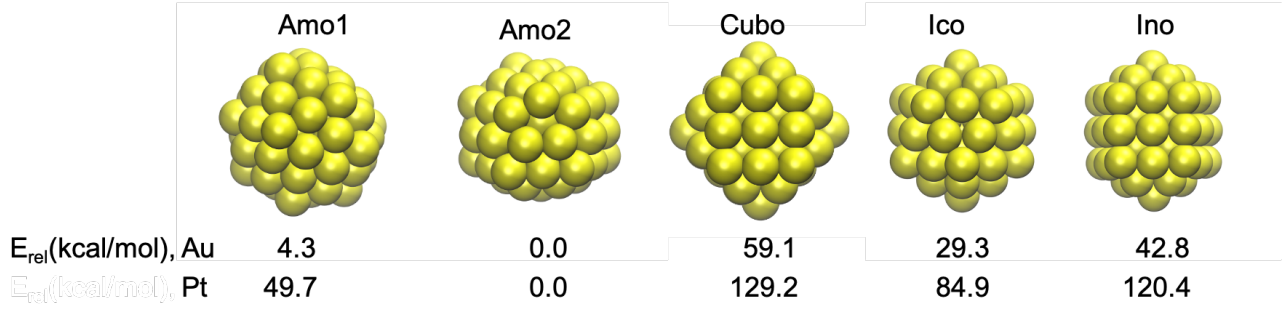

FIG. 7: Representation of considered Au_{55} geometries: The two amorphous (Amo) structures are lowest in energy, followed by the icosahedron (Ico), Ino's decahedron (Ino) and finally the cuboctahedron. Relative energies for the corresponding (reoptimized) Pt_{55} clusters are also given. Structures and energies are obtained by minimization at the DFT level using the PBE-dDsC functional.

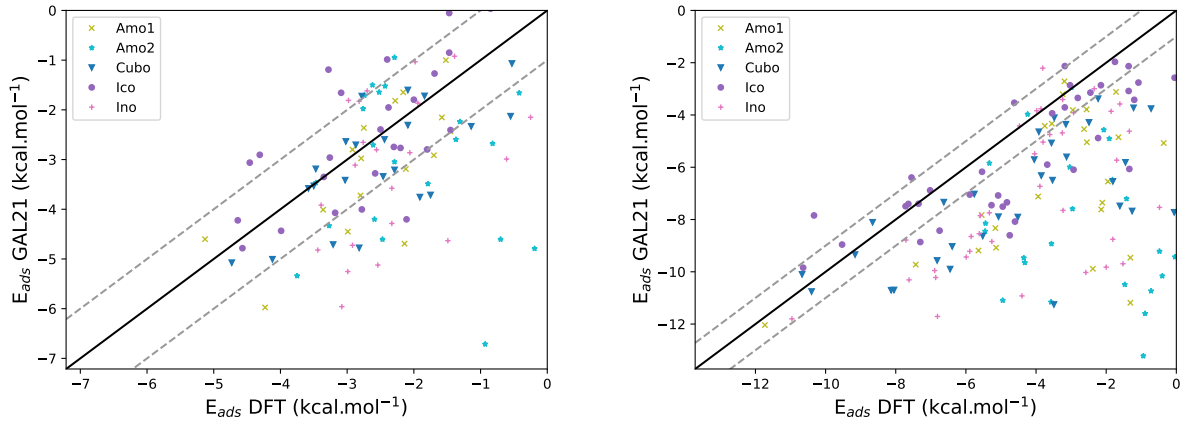

FIG. 8: Parity plot of GAL21 vs DFT for H_2O adsorption on five Au_{55} isomers (left) and Pt_{55} (right). The snapshots are extracted from fully solvated NPs. Only water molecules closer than 3.5 Å from a metal atom have been considered.

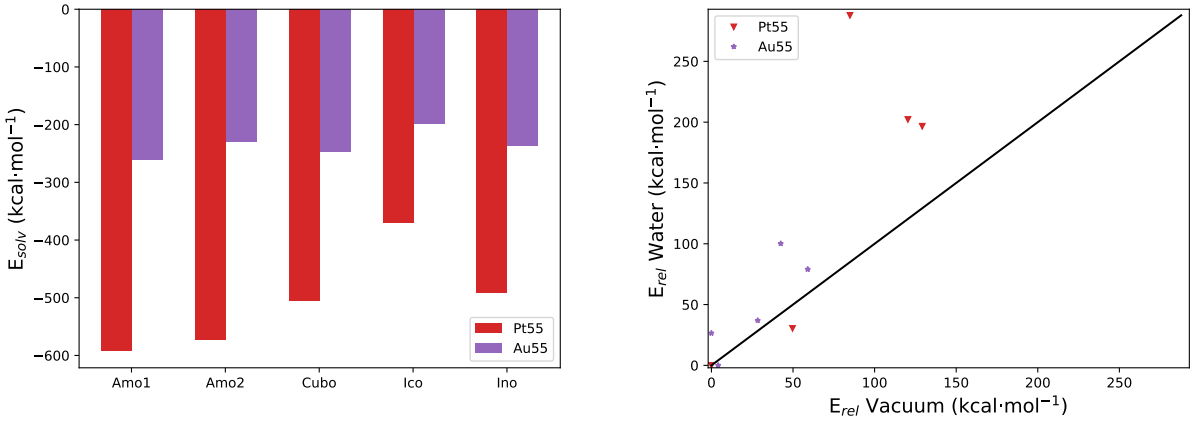

FIG. 9: Left: GAL21 solvation free energies for five Au_{55} and Pt_{55} isomers. Right: Parity plot of relative energy in solvent vs relative energy in vacuum for five Au_{55} and Pt_{55} isomers.

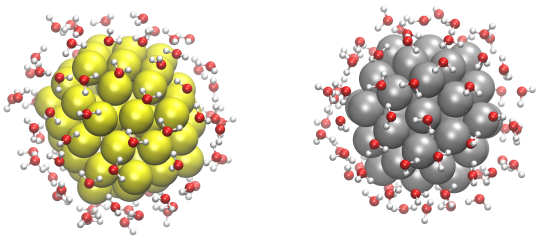

FIG. 10: Snapshot of the number of water molecules < 3.5 Å of the Au_{55Amo1} (left) and Pt_{55Ico} (right) nanoparticle.

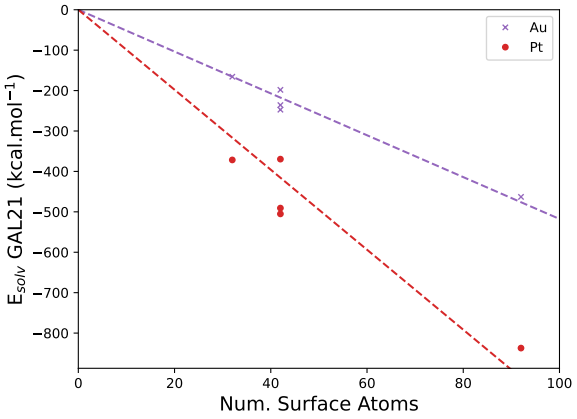

FIG. 11: Solvation energy of Au and Pt nanoparticles (38, 55 and 147 atoms) as a function of the surface atoms. The slope of the trend-line going through (0 atoms, 0 kcal·mol^{-1}) is -5.2 and -9.9 kcal·mol^{-1} per surface atom for Au and Pt, respectively.

that about 70 water molecules are within the 3.5 Å cutoff. Visual inspection for two extreme cases ("low" (Pt_{55Ico}) and "high" (Au_{55Amo1}) numbers of water molecules in this shell) shows that this 3.5 Å cutoff corresponds to the first solvation shell (see Fig. 10). The icosahedron being the most spherical shape investigated, its solvation shell includes the smallest number of water molecules. The difference is much more pronounced for Pt than for Au, but exists in both.

Now turning to the solvation free energy, Fig. 9 shows that platinum is much (2-3 times, see Figure S6) more solvated than gold. Note that error bars are not shown as they are at most 2 kcal·mol^{-1}, which amounts to less than 1% and would not be visible. Even though this trend is expected based on the adsorption energies, it is exacerbated compared to the single water adsorption energies, where the factor is about two (Fig. 5). Given that the number of water molecules found in the first solvation sphere is quite similar (Fig. S8), it is not obvious where this difference comes from. Furthermore, it should be noted that for the crystalline NPs (Cubo, Ico and Ino) the factor is roughly two, in agreement with expectations. Therefore, the "overstabilization" might be related to subtle geometrical changes that lower the GCNs of amorphous Pt_{55} compared to their Au_{55} analogs: Fig. S7 shows that the GCNs for amorphous Pt NPs are lower compared to their Au counterparts, even though we have not been able to identify a significant geometrical change by the naked eye.

Adding the DFT energy in vacuum to the solvation free energy, we can compute the relative stability in water of the five isomers and compare it to their stability in vacuum (see Fig. 9). Despite the very significant solvation energies, the relative energies in solution follow the ones in vacuum quite closely at least for the "low" (< 50 kcal·mol^{-1}) lying isomers. This can be understood given that the most stable (amorphous) isomers are also the ones that feature the lowest GCNs and the highest number of water molecules in the first solvation shell.

Finally, we also determine the solvation energy per surface atom. In order to do so, we estimate the surface atoms as the ones with GCNs < 8 and extend the investigated nanoparticles to a smaller one (38 atoms) and a larger one (147), both in a cuboctahedron shape. The results are shown in Fig. 11. As for the single water adsorption energy (Fig. 5) the solvation energy per surface atom of Pt is roughly twice as important as on Au (-9.9 vs -5.2 kcal·mol^{-1}). When compared to the estimate of the solvation energy of Pt(111) of Ref.[17] at the GAL17 level of theory of -5.2 kcal·mol^{-1} per surface atom, we note a significantly stronger solvation of the NPs. This is in agreement with the observation that the undercoordinated surface atoms interact more strongly with water. Furthermore, the corners and edges lead to less steric hindrance for the adsorbed water molecules compared to flat surfaces, so that comparably more water molecules can stabilize the surface.

In summary, the solvation energies of NPs in water are very large. In particular, the solvation energy per surface atom is in the order of -5 to -10 kcal·mol^{-1}. These solvation energies reduce the adsorption energies of molecules or ions on the NPs in water compared to the situation in gas-phase and can, therefore, not be neglected. For practical applications, GAL21 can be coupled to the SolvHybrid package of Ref.[17]. This QM/MM scheme allows to assess the effect of solvation on the adsorption of various species, including H* and OH* as a function of the morphology. However, according to our extensive sampling with a reasonably accurate force field, the water solvent does not induce a change in morphology, not even when water molecules are strongly interacting with the NPs.

VI. CONCLUSION

We have developed the third generation of the GAL force field, called GAL21. This pair-wise additive force field accounts for the morphology-dependent interaction

of metallic surfaces and nanoparticles via the generalized coordination number. The water adsorption is found to depend roughly quadratically on the GCN, with low GCNs leading to stronger adsorption. GAL21 achieves root mean square deviations of 1-2 kcal·mol^{-1} for seven metals, ranging from weakly (like Ag or Au) to strongly (like Ni or Pt) interacting metals. This force field, trained on (defective) single-crystal surfaces, is transferable to nanoparticles, even though GAL21 tends to overly stabilize water on amorphous NPs compared to DFT reference data. Finally, we have demonstrated the use of GAL21 for the determination of solvation energies of NPs. The solvation free energies of Pt NPs are 2-3 times more important than the ones for gold NPs, which can be rationalized by the stronger interaction energy of water with Pt compared to Au. For the systems investigated, the amorphous NPs are more stable in the gas-phase and feature at the same time lower GCNs than the crystalline ones. Together with the larger surface area and thus a larger solvation sphere, the solvation of the amorphous NPs is found to be stronger than for the crystalline ones. Hence, we do not have any evidence for a significant reordering of the relative energies between gas-phase and solution phase. Finally, we also assessed the solvation energy as a function of atoms exposed to the solvent. According to a linear regression on three sizes of NPs (from 38 to 147), the solvation energy for Au and Pt surface atoms are -5.2 and -9.9 kcal·mol^{-1}, respectively.

VII. SUPPLEMENTARY MATERIAL

Additional details on the training and validation set as well as additional Figures are available. Geometries can be retrieved online under the DOI of `10.17172/NOMAD/2022.10.28-1`.

ACKNOWLEDGMENTS

We are grateful to Paul Fleurat-Lessard for fruitfully discussions. The authors thank the SYSPROD project and AXELERA Pôle de Compétitivité for financial support (PSMN Data Center).

[1] J. Fan, Y. Cheng, and M. Sun, "Functionalized Gold Nanoparticles: Synthesis, Properties and Biomedical Applications," The Chemical Record **20**, 1474–1504 (2020).

[2] W. Roa, X. Zhang, L. Guo, A. Shaw, X. Hu, Y. Xiong, S. Gulavita, S. Patel, X. Sun, J. Chen, R. Moore, and J. Z. Xing, "Gold nanoparticle sensitize radiotherapy of prostate cancer cells by regulation of the cell cycle," Nanotechnology **20**, 375101 (2009).

[3] P. Hervés, M. Pérez-Lorenzo, L. M. Liz-Marzán, J. Dzubiella, Y. Lu, and M. Ballauff, "Catalysis by metallic nanoparticles in aqueous solution: model reactions," Chem. Soc. Rev. **41**, 5577–5587 (2012).

[4] G. Schmid, "Large clusters and colloids. Metals in the embryonic state," Chem. Rev. **92**, 1709–1727 (1992).

[5] N. Dimitratos, J. A. Lopez-Sanchez, and G. J. Hutchings, "Selective liquid phase oxidation with supported metal nanoparticles," Chem. Sci. **3**, 20–44 (2011).

[6] A. Corma and P. Serna, "Chemoselective Hydrogenation of Nitro Compounds with Supported Gold Catalysts," Science **313**, 332–334 (2006).

[7] A. Groß and S. Sakong, "Ab Initio Simulations of Water/Metal Interfaces," Chem. Rev. **122**, 10746–10776 (2022), publisher: American Chemical Society.

[8] S. Huang, T. M. Inerbaev, and D. S. Kilin, "Excited State Dynamics of Ru10 Cluster Interfacing Anatase TiO2(101) Surface and Liquid Water," J. Phys. Chem. Lett. **5**, 2823–2829 (2014).

[9] N. Siemer, D. Muñoz-Santiburcio, and D. Marx, "Solvation-Enhanced Oxygen Activation at Gold/Titania Nanocatalysts," ACS Catal. **10**, 8530–8534 (2020).

[10] C.-H. Chan, F. Poignant, M. Beuve, E. Dumont, and D. Loffreda, "A Water Solvation Shell Can Transform Gold Metastable Nanoparticles in the Fluxional Regime," J. Phys. Chem. Lett. **10**, 1092–1098 (2019).

[11] U. Benedikt, W. B. Schneider, and A. A. Auer, "Modelling electrified interfaces in quantum chemistry: constant charge vs. constant potential," Phys. Chem. Chem. Phys. **15**, 2712–2724 (2013).

[12] R. F. d. Morais, T. Kerber, F. Calle-Vallejo, P. Sautet, and D. Loffreda, "Capturing Solvation Effects at a Liquid/Nanoparticle Interface by Ab Initio Molecular Dynamics: Pt_{201} Immersed in Water," Small **12**, 5312–5319 (2016).

[13] B. Kirchhoff, L. Braunwarth, C. Jung, H. Jónsson, D. Fantauzzi, and T. Jacob, "Simulations of the oxidation and degradation of platinum electrocatalysts," Small **16**, 1905159 (2020).

[14] "Software for chemistry & materials (SCM)," Http://www.scm.com (accessed: September 2022).

[15] S. N. Steinmann and C. Michel, "How to Gain Atomistic Insights on Reactions at the Water/Solid Interface?" ACS Catal. **12**, 6294–6301 (2022).

[16] S. N. Steinmann, R. Ferreira De Morais, A. W. Götz, P. Fleurat-Lessard, M. Iannuzzi, P. Sautet, and C. Michel, "Force Field for Water over Pt(111): Development, Assessment, and Comparison," J. Chem. Theory Comput. **14**, 3238–3251 (2018).

[17] P. Clabaut, B. Schweitzer, A. W. Goetz, C. Michel, and S. N. Steinmann, "Solvation free energies and adsorption energies at the metal/water interface from hybrid quantum-mechanical/molecular mechanics simulations," J. Chem. Theory Comput. **16**, 6539 – 6549 (2020).

[18] A. K. Rappe, C. J. Casewit, K. S. Colwell, W. A. Goddard, and W. M. Skiff, "UFF, a full periodic table force field for molecular mechanics and molecular dynamics simulations," Journal of the American Chemical Society **114**, 10024–10035 (1992).

[19] P. Clabaut, P. Fleurat-Lessard, C. Michel, and S. N. Steinmann, "Ten facets, one force field: The GAL19 force field for water-noble metal interfaces," J. Chem. Theory Comput. **16**, 4565–4578 (2020).

[20] H. Heinz, R. A. Vaia, B. L. Farmer, and R. R. Naik, "Accurate Simulation of Surfaces and Interfaces of Face-Centered Cubic Metals Using 12-6 and 9-6 Lennard-Jones Potentials," J. Phys. Chem. C **112**, 17281–17290 (2008).

[21] F. Calle-Vallejo, J. I. Martínez, J. M. García-Lastra, P. Sautet, and D. Loffreda, "Fast Prediction of Adsorption Properties for Platinum Nanocatalysts with Generalized Coordination Numbers," Angewandte Chemie International Edition **53**, 8316–8319 (2014).

[22] F. Calle-Vallejo, R. F. de Morais, F. Illas, D. Loffreda, and P. Sautet, "Affordable Estimation of Solvation Contributions to the Adsorption Energies of Oxygenates on Metal Nanoparticles," The Journal of Physical Chemistry C **123**, 5578–5582 (2019).

[23] C. Marti, S. Blanck, R. Staub, S. Loehlé, C. Michel, and S. N. Steinmann, "Dockonsurf: A python code for the high-throughput screening of flexible molecules adsorbed on surfaces," J. Chem. Inf. Model. **61**, 3386–3396 (2021).

[24]K. Kaźmierczak, P. Clabaut, R. Staub, N. Perret, S. N. Steinmann, and C. Michel, "Designing Active Sites for Structure-Sensitive Reactions via the Generalized Coordination Number: Application to Alcohol Dehydrogenation," J. Phys. Chem. C **125**, 10370–10377 (2021).
[25]R. Staub and S. N. Steinmann, "Parameter-free coordination numbers for solutions and interfaces," The Journal of Chemical Physics **152**, 024124 (2020).
[26]K. T. Tang and J. P. Toennies, "An improved simple model for the van der Waals potential based on universal damping functions for the dispersion coefficients," J. Chem. Phys. **80**, 3726–3741 (1984).
[27]S. N. Steinmann and C. Corminboeuf, "A generalized-gradient approximation exchange hole model for dispersion coefficients," J. Chem. Phys. **134**, 044117 (2011).
[28]G. Kresse, "Ab initio molecular dynamics for liquid metals," J. Non-Cryst. Solids **192-193**, 222–229 (1995).
[29]G. Kresse and J. Furthmüller, "Efficient iterative schemes for *ab initio* total-energy calculations using a plane-wave basis set," Phys. Rev. B **54**, 11169–11186 (1996).
[30]J. P. Perdew, K. Burke, and M. Ernzerhof, "Generalized Gradient Approximation Made Simple," Phys. Rev. Lett. **77**, 3865–3868 (1996).
[31]S. N. Steinmann and C. Corminboeuf, "Comprehensive Benchmarking of a Density-Dependent Dispersion Correction," J. Chem. Theory Comput. **7**, 3567–3577 (2011).
[32]S. Gautier, S. N. Steinmann, C. Michel, P. Fleurat-Lessard, and P. Sautet, "Molecular adsorption at Pt(111). How accurate are DFT functionals?" Phys. Chem. Chem. Phys. **17**, 28921 (2015).
[33]P. E. Blöchl, "Projector augmented-wave method," Phys. Rev. B **50**, 17953–17979 (1994).
[34]G. Kresse and D. Joubert, "From ultrasoft pseudopotentials to the projector augmented-wave method," Phys. Rev. B **59**, 1758–1775 (1999).
[35]H. J. Monkhorst and J. D. Pack, "Special points for Brillouin-zone integrations," Phys. Rev. B **13**, 5188–5192 (1976).
[36]N. Tarrat, M. Rapacioli, J. Cuny, J. Morillo, J.-L. Heully, and F. Spiegelman, "Global optimization of neutral and charged 20- and 55-atom silver and gold clusters at the DFTB level," Computational and Theoretical Chemistry Structure prediction of nanoclusters from global optimization techniques: computational strategies, **1107**, 102–114 (2017).
[37]N. Abidi, A. Bonduelle-Skrzypczak, and S. N. Steinmann, "How Stable Are 2H-MoS_2 Edges under Hydrogen Evolution Reaction Conditions?" J. Phys. Chem. C **125**, 17058–17067 (2021).
[38]U. Borstnik, J. VandeVondele, V. Weber, and J. Hutter, "Sparse matrix multiplication: The distributed block-compressed sparse row library | Elsevier Enhanced Reader," Parallel Computing **40**, 47–58 (2014).
[39]J. Hutter, M. Iannuzzi, F. Schiffmann, and J. VandeVondele, "cp2k: atomistic simulations of condensed matter systems," WIREs Computational Molecular Science **4**, 15–25 (2014).
[40]U. Essmann, L. Perera, M. L. Berkowitz, T. Darden, H. Lee, and L. G. Pedersen, "A smooth particle mesh Ewald method," J. Chem. Phys. **103**, 8577–8593 (1995).
[41]G. Bussi, D. Donadio, and M. Parrinello, "Canonical sampling through velocity rescaling," J. Chem. Phys. **126**, 014101 (2007).
[42]William L. Jorgensen, J. Chandrasekhar, J. D. Madura, R. W. Impey, and M. L. Klein, "Comparison of simple potential functions for simulating liquid water," J. Chem. Phys. **79**, 926–935 (1983).
[43]H. Flyvbjerg and H. G. Petersen, "Error estimates on averages of correlated data," J. Chem. Phys. **91**, 461–466 (1989).
[44]A. Berg, C. Peter, and K. Johnston, "Evaluation and Optimization of Interface Force Fields for Water on Gold Surfaces," Journal of Chemical Theory and Computation **13**, 5610–5623 (2017).
[45]F. Iori, R. Di Felice, E. Molinari, and S. Corni, "Golp: An atomistic force-field to describe the interaction of proteins with au(111) surfaces in water," J. Comput. Chem. **30**, 1465–1476 (2009).
[46]F. Baletto, R. Ferrando, A. Fortunelli, F. Montalenti, and C. Mottet, "Crossover among structural motifs in transition and noble-metal clusters," J. Chem. Phys. **116**, 3856–3863 (2002).

	Co	Ni	Cu	Pd	Ag	Pt	Au
RMSD (kcal·mol^{-1})	1.28	1.58	1.05	1.11	0.73	1.40	0.72
n_{conf}	3513	3290	3945	3482	3114	3343	2977
R_O (Å)	2.098	2.287	2.120	2.142	2.378	2.177	2.224
$b_{\perp,0}$ (Å^{-2})	0.041	0.204	0.115	0.051	0.262	0.166	0.318
$b_{\perp,1}$ (Å^{-2})	0.1271	0.1133	0.1286	0.1071	0.0582	0.0905	0.0392
$b_{\parallel,0}$ (Å^{-2})	0.342	0.324	0.325	0.367	0.349	0.362	0.178
$b_{\parallel,1}$ (Å^{-2})	-0.0184	0.0317	-0.0098	-0.0111	-0.0247	-0.0004	-0.0039
B_0 (Å^{-1})	3.436	3.070	3.447	3.531	3.178	3.171	3.462
B_1 (Å^{-1})	0.0226	0.0325	-0.0390	-0.0018	-0.0249	-0.0069	-0.0615
$B_{H,0}$ (Å^{-1})	2.967	2.941	3.522	3.348	3.314	2.949	2.954
$B_{H,1}$ (Å^{-1})	0.0401	0.0881	0.0069	0.0841	0.1065	0.0585	0.0163
$a_{1,0}$ (kcal·mol^{-1})	-330.41	-194.44	-79.80	-105.59	-55.47	-65.49	-65.92
$a_{1,1}$ (kcal·mol^{-1})	109.88	73.65	33.36	38.54	21.78	27.73	33.50
$a_{1,2}$ (kcal·mol^{-1})	-7.93	-5.88	-2.56	-2.81	-1.70	-2.12	-2.85
$a_{2,0}$ (kcal·mol^{-1})	101.68	95.91	70.98	32.12	36.37	-45.18	48.35
$a_{2,1}$ (kcal·mol^{-1})	-32.73	-35.97	-19.54	-10.33	-8.86	20.57	-18.39
$a_{2,2}$ (kcal·mol^{-1})	2.47	2.91	1.33	0.82	0.53	-1.74	1.57
$a_{3,0}$ (kcal·mol^{-1})	-49.87	-109.66	-100.15	-88.67	-47.49	-88.65	-31.93
$a_{3,1}$ (kcal·mol^{-1})	9.83	32.08	22.26	28.30	12.19	28.11	5.50
$a_{3,2}$ (kcal·mol^{-1})	-0.50	-2.20	-1.14	-2.12	-0.71	-2.05	-0.09
$a_{4,0}$ (kcal·mol^{-1})	4.24	10.60	20.14	16.39	7.82	29.54	-1.64
$a_{4,1}$ (kcal·mol^{-1})	0.00	0.00	0.00	0.00	0.00	0.00	0.00
$a_{4,2}$ (kcal·mol^{-1})	-0.08	-0.20	-0.37	-0.35	-0.13	-0.56	0.07
$\varepsilon_{a,0}$ (kcal·mol^{-1})	-0.031	-4.023	0.298	0.766	0.415	0.632	-0.230
$\varepsilon_{a,1}$ (kcal·mol^{-1})	-10.40	44.87	-10.78	-17.65	-11.53	-18.21	1.63
$\varepsilon_{a,2}$ (kcal·mol^{-1})	92.80	64.15	84.35	130.56	76.32	200.00	12.89
A_0 (kcal·mol^{-1})	8198.02	4527.04	9901.00	30386.07	12833.18	16757.08	12928.33
A_1 (kcal·mol^{-1})	2336.13	2518.75	0.00	259.78	0.00	723.45	0.00
$A_{H,0}$ (kcal·mol^{-1})	2937.29	1805.49	6506.64	3219.69	5544.04	2211.10	2580.41
$A_{H,1}$ (kcal·mol^{-1})	112.83	352.13	14.71	1544.04	2378.06	446.63	70.45
C (Å^6·kcal·mol^{-1})	1243	1241	1250	1229	1690	1589	1632

TABLE I: RMSD, number of configurations with negative adsorption energies, non-linear fitted parameters, linear fitted parameters and C which is directly taken from the dDsC dispersion correction used in the DFT reference energies.